Dynamic densification behavior of nanoiron powders under shock compression

C. D. Dai, D. E. Eakins, and N. N. Thadhani[a)]
School of Materials Science and Engineering, Georgia Institute of Technology, Atlanta, Georgia 30332, USA

(Received 5 January 2008; accepted 19 February 2008; published online 2 May 2008)

The dynamic densification behavior of nanoiron powder (~25 nm particle size) prepressed to ~35% and ~45% of solid density was determined based on measurements of shock input stress and wave velocity by using piezoelectric stress gauges. The experimentally determined shock densification response is observed to be sensitive to the initial density (or porosity) of prepressed nanoiron powder compacts. Hugoniot measurements show an obvious densification-distension transition at ~2 GPa for the ~35% dense and ~6 GPa for the ~45% dense powder compacts. The densification and shock compression responses of the nanoiron powders are also calculated by using isobaric and isochoric models. Correlations of the model calculations with the measured data indicate that the shock Hugoniot of nanoiron powders cannot be correctly described by the currently available analytical models that are otherwise capable of predicting the Hugoniot of highly porous materials (prepressed compacts) of micron-sized powders. © *2008 American Institute of Physics*. [DOI: 10.1063/1.2908209]

I. INTRODUCTION

The shock compression (Hugoniot) behavior of distended materials (e.g., porous media and powder compacts) is of significant interest due to their shock dissipation properties in engineering applications,[1] as an approach for fabricating bulk materials via consolidation of powders,[2,3] and for developing a complete equation of state (EOS) over a wide range of state variables.[4] The densification response of nanosized powder particles is of even greater interest for energetic or other applications since the effects of their high surface area can make it challenging to attain interparticle bonding, and the internal energy of the system can be dominated by the large surface energy contribution of the nanosized powder particles.[5] The shock compression behavior or Hugoniot (loci of final shock states) of nanosized powder particles has not been experimentally measured. Obviously, it is also not always practical to measure the shock Hugoniot for powders or distended materials of wide range of porosities. Thus, several analytical methods, such as those proposed by McQueen *et al.*,[6] Simon–Legner,[7] Oh–Persson,[8] Dijken–De Hosson,[9] Wu–Jing,[10] and Viljoen *et al.*,[11] have been developed to predict the Hugoniot of distended materials or powder compacts of various densities.

Most analytical models predict the porous response mainly based on the known shock Hugoniot of the corresponding solid material. The approaches utilized in these analytical models can be roughly classified into two types: (a) isochoric approach such as that used in the model of McQueen *et al.*,[6] in which the pressure at any specific volume is obtained from its solid Hugoniot via the Grüneisen EOS, and (b) isobaric approach such as that used in Wu–Jing's model,[10] in which the specific volume at any given pressure is acquired from its solid Hugoniot via the Wu–Jing EOS.[10] Models based on the isochoric conditions cannot be used to evaluate the Hugoniot in the incomplete (partial) compaction region, while those based on the isobaric conditions can be employed to describe the shock compression or densification response of distended materials with different initial porosities in both complete and incomplete compaction regions. The P-α (Refs. 12 and 13) and the P-λ (Refs. 14 and 15) models are also based on the isobaric approach but are not capable of predicting the shock Hugoniot, although these models can describe or fit experimental data.

The models of McQueen *et al.* and Wu–Jing, which are, respectively, representative of isochoric and isobaric approaches based models, are capable of predicting the Hugoniot of distended materials.[6,10,11] Both models, however, neglect the difference in specific internal energy between the distended material and the corresponding polycrystalline solid at identical pressure or specific volume. Hence, it is uncertain if the two models can still be applicable for predicting the Hugoniot of prepressed nanopowder compacts, which have a large specific surface energy contribution relative to the specific internal energy. There exist no Hugoniot data for nanosized powder compacts available for model validation.

In this paper, we briefly review the models of McQueen *et al.* and Wu–Jing and show the decreasing accuracy of both models in predicting the Hugoniot of highly porous solids (or powder compacts) by comparing those with experimental data available from literature. Then, we describe the results of measurements of the shock Hugoniots of nanoiron (~20 nm average size) powder prepressed to ~35% and ~45% of solid density ρ_o [also known as theoretical maximum density (TMD)] and compare those to the predicted results from calculations performed by using the models of McQueen *et al.* and Wu–Jing.

a)Author to whom correspondence should be addressed. Electronic mail: naresh.thadhani@mse.gatech.edu.

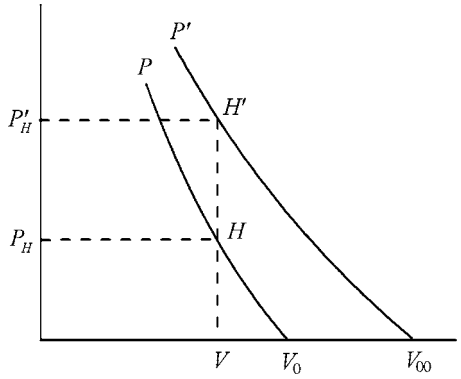

FIG. 1. Schematic illustrating the porous and solid Hugoniots on the $P-V$ plane. H and H' are the points on the solid Hugoniot $(P-V_0)$ and porous Hugoniot $(P'-V_{00})$, respectively. The HEL or strength of the porous material and solid is neglected.

II. REPRESENTATIVE MODELS FOR PREDICTING POROUS HUGONIOT

A. The isochoric model of McQueen *et al.*

By utilizing the Hugoniot for a solid of identical composition as the reference, the pressure (P'_H) of a specified distended material at any given specific volume (V) illustrated in Fig. 1, can be obtained by means of the Grüneisen EOS expressed as

$$P'_H = \left[\frac{1-(\gamma/V)(V_0-V)/2}{1-(\gamma/V)(V_{00}-V)/2}\right]P_H + \frac{(\gamma/V)(E_{00}-E_0)}{1-(\gamma/V)(V_{00}-V)/2}, \tag{1}$$

where P_H is the shock pressure at H under $V=V_H=V'_H$, V_{00} $(=1/\rho_{00})$ and V_0 $(=1/\rho_0)$ are the initial specific volumes of the distended material and the solid, respectively, E_{00} and E_0 are the specific internal energies of the distended material and the solid at ambient conditions, and γ is the Grüneisen parameter under shock compression. In the derivation of Eq. (1), the value of Grüneisen parameter γ at isochoric conditions is assumed to be identical for the distended material and the solid. If the approximation $E_{00}\approx E_0$ is considered, then Eq. (1) reduces to the expression of McQueen *et al.*,[6]

$$P'_H = \left[\frac{1-(\gamma/V)(V_0-V)/2}{1-(\gamma/V)(V_{00}-V)/2}\right]P_H. \tag{2}$$

Given any shock pressure P_H, one can determine a corresponding P'_H at $V=V_{H'}=V_H$ on the porous Hugoniot by using Eq. (2). The corresponding shock wave velocity D' and particle velocity u' of the distended material can also be determined by using

$$D' = V_{00}\sqrt{P'_H/(V_{00}-V)}, \tag{3}$$

$$u' = \sqrt{P'_H(V_{00}-V)}. \tag{4}$$

Equation (2) requires that $(\gamma/V)(V_{00}-V)/2\neq 1$, namely, $V/V_{00}\neq 1/(1+2/\gamma)$, implying that it is not possible to compress the distended material to the specific volume of $V_{00}/(1+2/\gamma)$. Furthermore, Eqs. (2)–(4) require

$$1-(\gamma/V)(V_0-V)/2\geqslant 0,$$

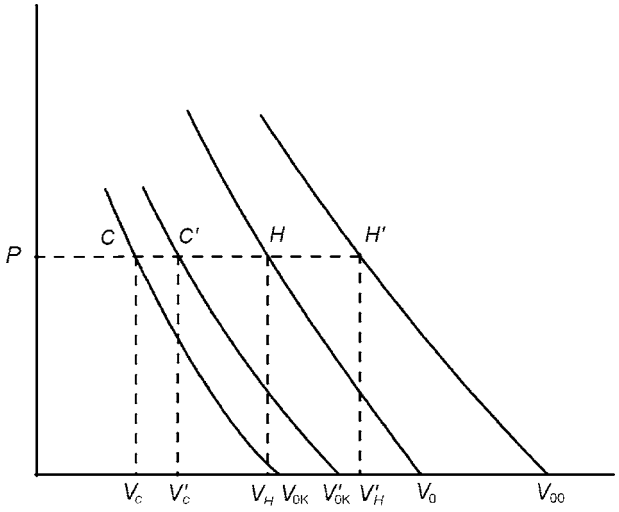

FIG. 2. Schematic illustrating the 0 K isotherm and Hugoniot of the porous material and the corresponding solid. C' and C, respectively, denote the point on the 0 K isotherms of the porous material and solid; H' and H represent the point on the Hugoniots of the porous material and solid, respectively; P_C and V_C, P'_C and V'_C, P_H and V_H, and P'_H and V'_H are, respectively, the pressure and specific volume at C, C', H, and H'; V_{00} and V_0 are, respectively, the initial specific volume of the porous material and solid; $V_{0\,\mathrm{K}}$ and $V'_{0\,\mathrm{K}}$ are, respectively, the initial specific volume on the 0 K isotherm, $P_C=P'_C=P_H=P'_H=P$. The HEL of the porous and solid Hugoniots or material strength is neglected.

$$V_{00}-V\geqslant 0 \tag{5a}$$

or

$$1-(\gamma/V)(V_0-V)/2\leqslant 0,$$

$$1-(\gamma/V)(V_{00}-V)/2<0,$$

$$V_{00}-V\geqslant 0. \tag{5b}$$

Equation (5a) and (5b) constrains $V_{00}/(1+2/\gamma)<V<V_{00}$ or $V<V_0/(1+2/\gamma)$. Actually, the shock states in the range of $V<V_0/(1+2/\gamma)$ are not always reached in Hugoniot experiments of distended materials. Thus, Eq. (2) is usually used to predict the porous Hugoniot in the range of $V_{00}/(1+2/\gamma)<V<V_{00}$ or $\rho_{00}<\rho<\rho_{00}(1+2/\gamma)$. Accordingly, the method of McQueen *et al.* is sufficient only with initial density $\rho_{00}\rho_0/(1+2/\gamma_0)$ or porosity $\alpha_0<1+2/\gamma_0$ (where the porosity $\alpha_0=V_{00}/V_0=\rho_0/\rho_{00}$ and γ_0 is the Grüneisen constant at ambient conditions). In fact, an abnormal Hugoniot is obtained as $\rho_{00}<\rho_0/(1+2/\gamma_0)$, in which case the specific volume increases with increasing pressure.[16] Experimental data for porous materials with low porosity are found to be in good agreement with predicted results[6,17] by using the method of McQueen *et al.*, suggesting that the approximations in this model are basically reasonable and reliable in the case of porosity $\alpha_0<1+2/\gamma_0$.

B. Wu–Jing's isobaric model

By employing the solid Hugoniot and 0 K isotherms of the solid and porous materials as the references, the specific volume (V'_H) at any given pressure (P) illustrated in Fig. 2

TABLE I. Solid Hugoniot data and relevant parameters used in model calculations for predicting porous Hugoniots. The parameters include ρ_0 as the solid or theoretical density, $V_{0\,\mathrm{K}}$ as the initial specific volume of solid at 0 K, C_0 as the bulk sound velocity, and Q and q as the constants for the Born–Mayer potential [Eq. (8)] directly determined from the solid Hugoniot; likewise, Y is a constant corresponding to the strength of the matrix material [Eq. (9)].

Materials	ρ_0 (g/cm^3)	$V_{0\,\mathrm{K}}$ (cm^3/g)	C_0 (km/s)	γ_0[a]	Q (GPa)	q	Y[b] (GPa)
2024 Al	2.785[a]	0.35218[c]	5.328[a]	2.0	37.890[c]	8.419[c]	0.2
Cu	8.93[d]	0.11050[e]	3.933[d]	1.96	59.717[e]	9.889[e]	0.1
Fe	7.85[f]	0.12563[e]	3.935[f]	1.69	39.960[e]	11.280[e]	0.5

[a]See Ref. 19.
[b]Reference 20.
[c]See Ref. 10.
[d]See Ref. 21.
[e]Reference 22.
[f]Reference 23.

can be expressed as[10]

$$V'_H = \frac{(1-R/2)V_H}{1-(R/2)(1-P_E/P)} + \frac{(R/2)[V_E - V_0 + P_E V_{00}/P + 2(1-R)(V'_C - V_C)/R]}{1-(R/2)(1-P_E/P)}, \tag{6}$$

where V_H is the specific volume on the solid Hugoniot at $P=P_H$, P_E and V_E are the pressure and specific volume at the Hugoniot elastic limit (HEL) of the porous material, respectively, V_{00} and V_0 are the initial specific volumes of the porous material and the solid, respectively, V'_C and V_C are the specific volumes on the 0 K isotherm of the porous material and the solid, respectively, the R is a pressure-dependent parameter described by[10]

$$R = P(\partial V/\partial H)_P = (P/C_P)(\partial V/\partial T)_P = P\gamma/K_S, \tag{7}$$

where C_P, γ, and K_S are the constant-pressure heat capacity, Grüneisen parameter, and bulk modulus at high pressure, respectively. R is treated as a parameter with the same value for both the solid and porous materials under isobaric condition. In the derivation of Eq. (6), the specific internal energy is also assumed to be the same for both the porous material and the solid under isobaric conditions.[10]

The specific volume (V_C) on the 0 K isotherm of solid at $P_C=P_H$ is obtained in Wu–Jing's method based on the Born–Mayer potential[18]

$$P_C = Q(V_{0\,\mathrm{K}}/V_C)^{2/3}(\exp\{q[1-(V_{0\,\mathrm{K}}/V_C)^{-1/3}]\} - (V_{0\,\mathrm{K}}/V_C)^{2/3}), \tag{8}$$

where Q and q are two material constants that can be determined from the known solid Hugoniot and $V_{0\,\mathrm{K}}$ is the initial specific volume of the solid at 0 K. To determine the V'_C on the 0 K isotherm of the porous material at isobaric conditions, Wu and Jing[10] introduced a parameter $\alpha_C = V'_C/V_C$, which is approximately described by using the simplified Carroll–Holt model,[13]

$$\alpha_C \approx \alpha_0 \quad \text{for } 0 < P < P_{\mathrm{crit}},$$

$$\alpha_C \approx 1/[1-\exp(-3P/2Y)] \quad \text{for } P > P_{\mathrm{crit}}, \tag{9}$$

where $\alpha_0 = V_{00}/V_0$ and Y and P_{crit} are the strength of the matrix material and the elastic critical pressure of porous material respectively. Generally, the values for P_E and Y for the porous material are lower than the shock load. If the shock load is high enough, we have $V'_C \to V_C$, $P_E/P \to 0$, and $V_E \approx V_{00}$. Hence, in the case of intense shock loading, Eq. (6) reduces to

$$V'_H = V_H + \frac{(R/2)(V_{00}-V_0)}{1-R/2}. \tag{10}$$

Equation (10) requires that $R \neq 2$. Actually, $R < \frac{1}{2}$ for typical metals or alloys in the pressure range of a few hundreds of gigapascals.[10]

C. Model calculations

By using the methods of McQueen *et al.* and Wu–Jing, methods, we calculated the Hugoniot of three representative metals (2024 aluminum, copper, and iron) for which the experimentally determined Hugoniot for various densities was available in the literature.[19] The calculated results were compared to the available experimental data to determine the applicability of the models as a function of decreasing density. The values of relevant parameters[19–23] used in model calculations are given in Table I. The empirical parametrization[6] of $\rho\gamma \approx \rho_0\gamma_0$ was used for both model calculations. The difference in results from the Wu–Jing model calculations using Eqs. (6) and (10) is very slight and even unidentified in the complete compaction region for these porous metals (all the experimental data[19] for model validations are located in the complete compaction region), which indicated that Eq. (10) is a good approximation to Eq. (6) in the complete compaction region.

The predicted D-u, P-u, and $P-V/V_{00}$ Hugoniots for porous 2024 Al of $\alpha_0 \approx 1.25$ ($\rho_{00}=79.8\%$ TMD) and $\alpha_0 \approx 1.68$ ($\rho_{00}=59.6\%$ TMD) correlated with the available experimental data[19] are shown in Fig. 3. It is seen that the predicted Hugoniot for porous 2024 Al of $\alpha_0 \approx 1.25$ using either the the method of McQueen *et al.* or Wu–Jing's is

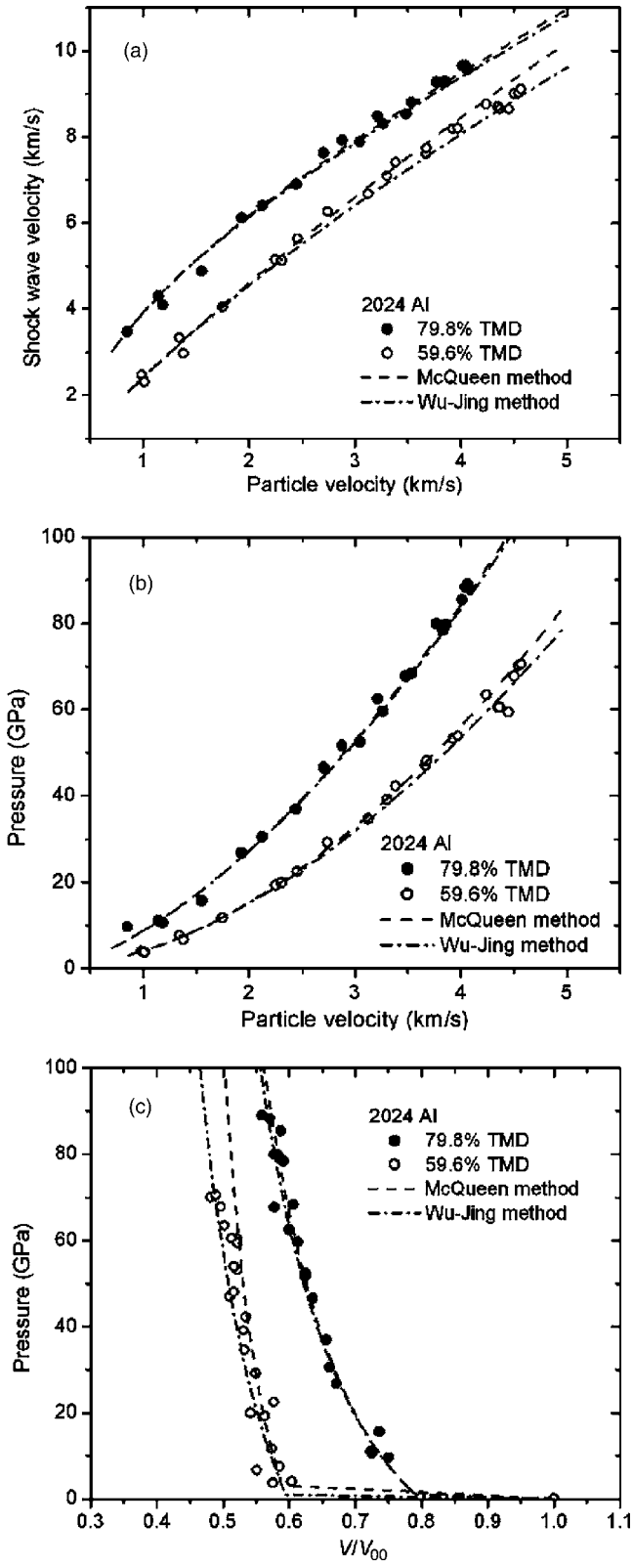

FIG. 3. Calculated Hugoniot for porous 2024 Al compared to available experimental data (Ref. 19). (a) D-u, (b) P-u, and (c) $P-V/V_{00}$.

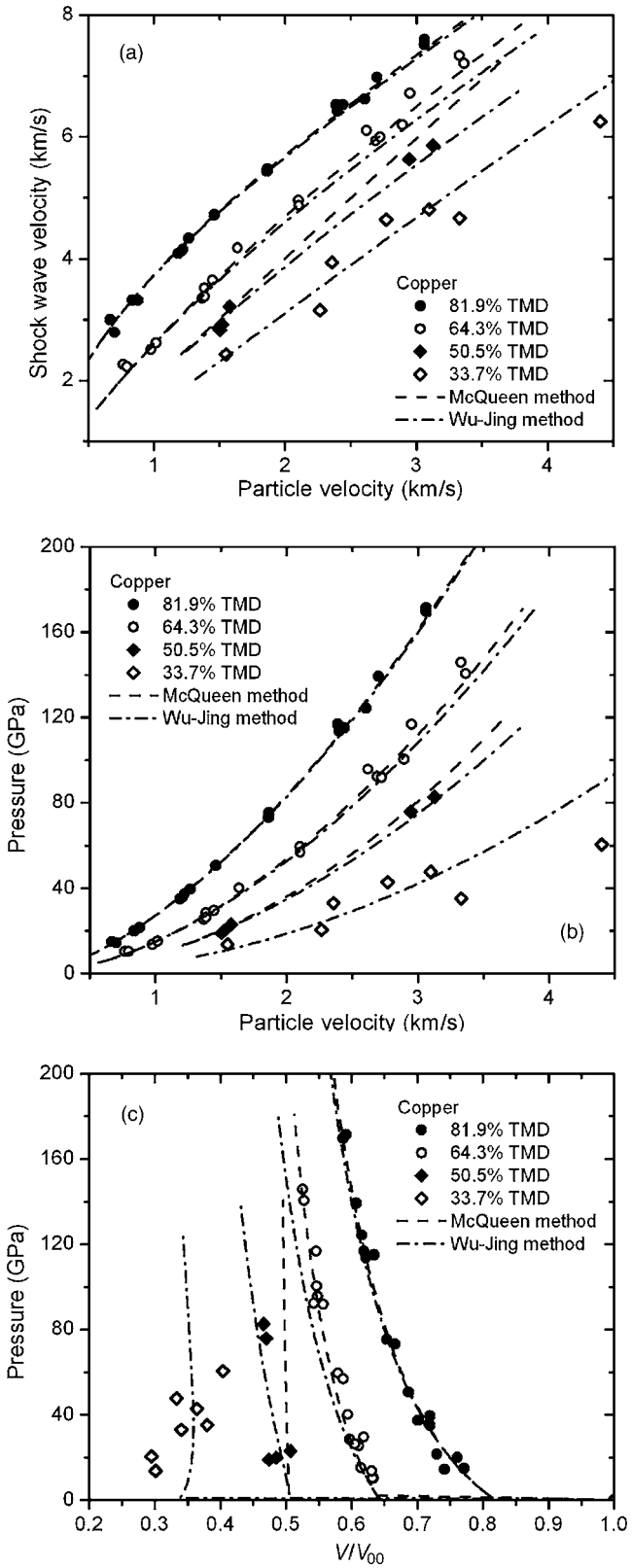

FIG. 4. Calculated Hugoniot for porous copper compared to available experimental data (Ref. 19). (a) D-u, (b) P-u, and (c) $P-V/V_{00}$.

consistent with the experimental data, and the consistency decreases to a certain degree as the porosity increases to $\alpha_0 \approx 1.68$.

The predicted Hugoniots of porous Cu with $\alpha_0 \approx 1.22$ (81.9% TMD), $\alpha_0 \approx 1.56$ (64.3% TMD), $\alpha_0 \approx 1.98$ (50.5% TMD), and $\alpha_0 \approx 2.97$ (33.7% TMD) are plotted in Fig. 4 in comparison to the available experimental data.[19] It is obvious that the method of McQueen *et al.* does not predict the porous Hugoniot as $\alpha_0 > 1+2/\gamma_0$ (≈ 2.02 for porous Cu). The predicted $P-V/V_{00}$ Hugoniot for porous Cu of $\alpha_0 \approx 1.98$ using the McQueen *et al.* method is almost a vertical line since

the initial porosity almost reaches the critical value of porosity $(1+2/\gamma_0 \approx 2.02)$. On the other hand, the predicted Hugoniot for porous Cu of $\alpha_0 \approx 2.97$ using Wu–Jing's method is approximately consistent with available experimental data within the uncertainty of measurements. The comparison illustrates that the Wu–Jing model is still capable of predicting the Hugoniot for porous Cu of $\alpha_0 \approx 2.97$ over the critical value of porosity.

The predicted Hugoniots for porous Fe of $\alpha_0 \approx 1.13$ (88.8% TMD), $\alpha_0 \approx 1.31$ (76.2% TMD), $\alpha_0 \approx 1.66$ (60.4% TMD), and $\alpha_0 \approx 2.33$ (42.9% TMD) are given in Fig. 5, along with the available experimental data.[19] It is observed that the predicted results using both the methods of McQueen *et al.* and the Wu–Jing are consistent with available experimental data for porous Fe of $\alpha_0 \approx 1.13$ and $\alpha_0 \approx 1.31$. However, there exists obvious deviation of predicted results from the experimental data as α_0 increases to 1.66 (60.4% TMD) and 2.33 (42.9% TMD), indicating that the accuracy of predicted Hugoniots decreases with increasing porosity.

The assumptions in the model of McQueen *et al.* mainly include the following: (a) the specific internal energy at initial conditions is identical for both the porous material and the solid and (b) the Grüneisen parameter γ has the same value for the porous material and solid at identical specific volume. Similarly, the assumptions in the Wu–Jing model principally include the following: (a) the specific internal energy is the same for both the porous material and the solid at identical pressure and (b) the pressure-dependent parameter R associated with the Grüneisen parameter γ is identical in value for the porous material and the solid at the same pressure. Hence, for powder compacts of nanoscale (tens to a few nanometers) particles, neglecting the difference in the specific internal energy between the nanoparticles and the solid can potentially result in large deviation between the predicted results and the real case because nanoparticles possess a much larger specific surface energy, which can more significantly influence the specific internal energy, relative to that for the micron-sized powders. In addition, neglecting the difference in the Grüneisen parameter γ under isochoric conditions can also potentially result in a large deviation because the lattice vibrations in nanoparticles associated with the Grüneisen parameter γ are influenced to a certain degree by the interfaces of nanoparticles (size effect).[24] The comparison of the predicted Hugoniots for porous 2024 Al, Cu, and Fe with the available experimental data clearly show that the deviation of predicted results with experimental data are generally increasing with increasing porosity, which is linked to the effects of the specific internal energy and other thermodynamic properties. In more recent works,[25,26] the Wu–Jing model[12] has been extended by the authors to incorporate thermal pressure of electrons and correlate the calculated Hugoniot of highly porous metals including tungsten, copper, iron, lead, and aluminum, with experimental data available in the Russian literature. While good overall agreement has been demonstrated, the model still neglects the thermal pressure contribution from the lattice, which can be quite significant in the case of shock densification of nanoparticles.

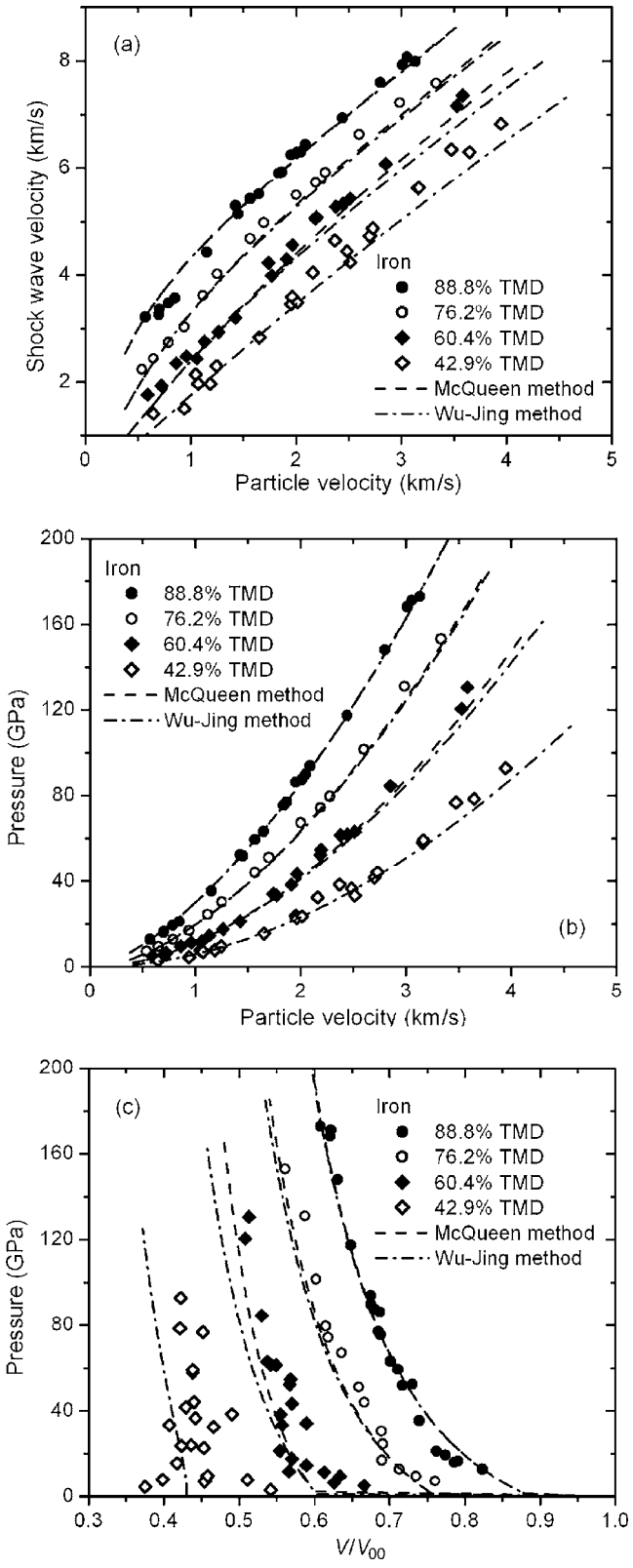

FIG. 5. Calculated Hugoniot for porous iron compared to available experimental data (Ref. 19). (a) D-u, (b) P-u, and (c) $P-V/V_{00}$.

III. HUGONIOT EXPERIMENTS ON NANOIRON POWDER COMPACT

The Hugoniot of the nano-Fe powder compact was measured by using polyvinylidene fluoride (PVDF) piezoelectric stress gauges. Commercially available nanosized powder of

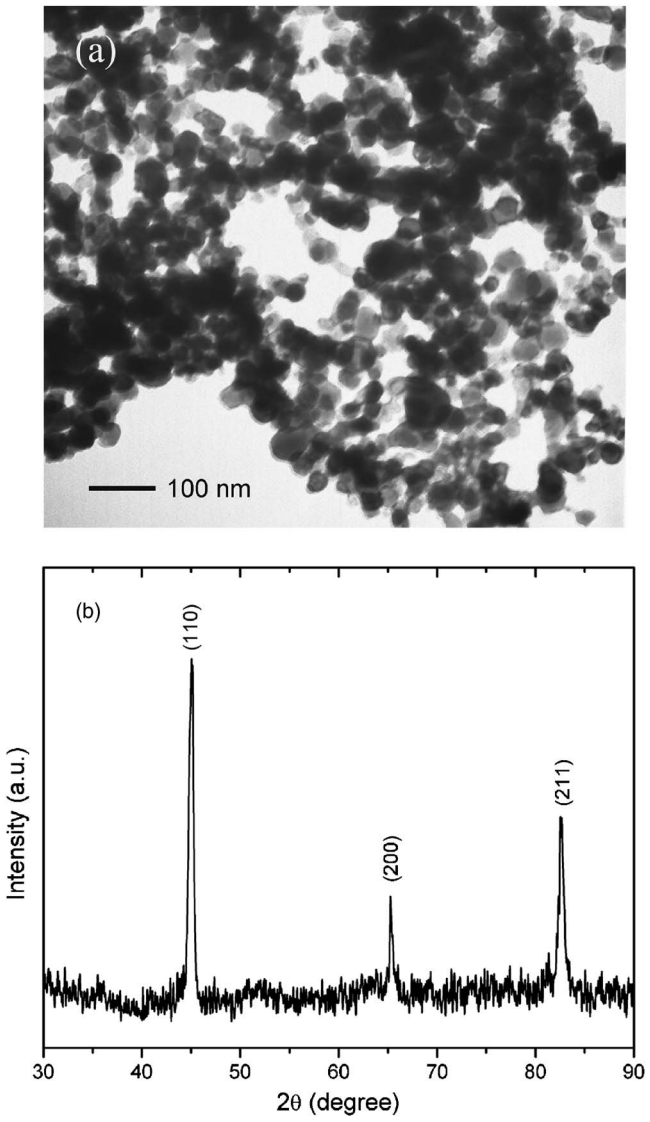

FIG. 6. Commercially available nanoiron powder used for Hugoniot experiments. (a) Morphology of spherical nanoiron particles with peak size distribution of ~25 nm. (b) XRD pattern showing the characteristic peaks of iron without any obvious impurity phases or oxide contaminants.

~25 nm Fe particles was obtained from Nanostructured & Amorphous Materials, Inc. Figure 6 shows the morphology (a) and x-ray diffraction pattern (b) of the nano-Fe particles, which have a peak size distribution of ~25 nm and a TMD of ~7.85 g/cm^3. Hugoniot measurements were performed on the nanoiron powders prepressed to ~35% TMD ($\alpha_0 \approx 2.86$) and ~45% TMD ($\alpha_0 \approx 2.22$). For the ~35% TMD compact (~50.8 mm in diameter, thickness slightly varied for different shots, see Table II), the nano-Fe powder was directly pressed against a copper driver plate and ring assembly. For ~45% TMD compact (~31.8 mm in diameter, thickness slightly varied for different shots, see Table II), the nano-Fe powder was pressed in a steel punch-and-die set to the desired density and then placed in the copper driver plate and ring assembly. Each powder compact was backed by a disk of polymethyl methacrylate (PMMA) (~16.9 mm in height). The packing and pressing of the powders were performed in argon gas to prevent contamination of the Fe nanoparticles. Commercially acquired PVDF piezoelectric stress gauges[27] (S25_09 shock gauges of a 3×3 mm^2 element obtained from Ktech Corporation) were embedded, respectively, between the Cu driver and the powder compact interface to measure the input stress and between the powder and PMMA backer to measure the propagated stress. The assembly is shown schematically in Fig. 7. The input and propagated gauges sandwiching the sample of known thickness also allowed a measurement of the shock wave velocity in the nanopowder compact based on the shock travel time between the two gauges.

The PVDF gauge packages consisting of an insulating film of Teflon (~25 μm thick) on both sides of an ~25 μm thick PVDF element were epoxy mounted with a bond thickness of 2–4 μm. Aluminum deposition of ~150 nm on the powder compact sides of the gauge package was utilized to prevent pyroelectric effects from affecting the gauge response during shock loading. The projectile velocity was measured by using four in-line shorting pins. The piezoelectric stress gauge was connected to a current viewing resistor and recorded on a digital oscilloscope with a sampling rate of 1 GHz. The PVDF gauges provided a current-time profile of 1 ns resolution, which was then numerically integrated to obtain the stress-time trace. The 80 mm diameter single-stage light-gas gun at Georgia Tech was utilized for performing the shock experiments. Copper (~57 mm diameter and ~9.5 mm thickness) or tungsten heavy alloy (WHA, ~57 mm diameter and ~5.2 mm thick) was used as the flyer plate to acquire the desired shock stress in the sample. The details of the experimental procedures, measurement method, and data analysis are described in more detail elsewhere.[28]

IV. RESULTS AND DISCUSSION

A series of 12 impact experiments (6 each for ~35% TMD and ~45% TMD compacts) were performed on nano-Fe powders, in which the shock input and propagated stress history and the shock wave propagation velocity were measured. Figure 8 shows input and propagated stress traces on the same plot for representative Hugoniot experiments performed on (a) ~35% TMD and (b) ~45% TMD nano-Fe powder compacts. For the ~35% TMD powder compact (shot 0661), the input stress trace shown in Fig. 8(a) reveals a second-step plateau due to reshock or recompression to higher stress, indicating that this sample is of lower shock impedance than the PMMA backer. For the ~45% TMD powder compact (shot 0732), the input stress shown in Fig. 8(b) reveals a release in stress following the shock duration, indicating that this sample is of higher shock impedance relative to the PMMA backer at the loaded stress level.

The method for the determination of the equilibrated (within 5–150 ns) input and propagated stresses and shock velocity, consistent with the approach employed in previous studies,[29–32] is illustrated in Fig. 9, which provides an example of the voltage and stress traces recorded by the corresponding [(a) and (b)] input gauge and [(c) and (d)] propagated gauge for shot 0661. As the forward-going shock wave [Fig. 9(a)] travels through the input gauge package (with ~25 μm Teflon insulation film on each side) and into the

TABLE II. Data obtained from Hugoniot experiments for the ~25 nm Fe powder compacts of ~35% TMD and ~45% TMD. ρ_{00}, initial density of compact; Δh, compact thickness; W, impact velocity; $\sigma_{x,\text{input}}$, input stress; $\sigma_{x,\text{prop}}$, propagated stress; Δt, transit time; D, shock wave velocity; u, particle velocity; ρ, shock-compressive density, $V=1/\rho$; V_0, initial specific volumes of Fe solid. Uncertainties are the standard deviations.

Shot No.	ρ_{00} (g/cm^3)	Δh (mm)	W (m/s)	$\sigma_{x,\text{input}}$ (GPa)	$\sigma_{x,\text{prop}}$ (GPa)	Δt (μs)	D (km/s)	u (km/s)	ρ (g/cm^3)	V/V_0
0655	2.760 ±0.032	2.062 ±0.012	780 (Cu)[a]	2.5 ±0.1	[b]	1.570 ±0.018	1.313 ±0.017	0.690 ±0.030	5.816 ±0.301	1.350 ±0.070
0661	2.758 ±0.031	2.294 ±0.013	947 (Cu)	3.0 ±0.1	3.7 ±0.1	1.571 ±0.010	1.460 ±0.012	0.745 ±0.027	5.630 ±0.227	1.394 ±0.056
0662	2.762 ±0.029	2.350 ±0.015	1018 (WHA)	4.2 ±0.2	[b]	1.309 ±0.006	1.795 ±0.014	0.847 ±0.042	5.230 ±0.240	1.501 ±0.069
0663	2.756 ±0.032	2.197 ±0.011	708 (Cu)	2.1 ±0.1	2.6 ±0.1	1.867 ±0.023	1.177 ±0.016	0.648 ±0.033	6.128 ±0.400	1.281 ±0.084
0671	2.748 ±0.035	2.491 ±0.016	501 (Cu)	1.1 ±0.1	1.6 ±0.1	2.432 ±0.010	1.024 ±0.008	0.391 ±0.036	4.443 ±0.260	1.767 ±0.103
0672	2.729 ±0.047	2.400 ±0.020	621 (Cu)	1.4 ±0.1	1.9 ±0.1	2.171 ±0.016	1.105 ±0.012	0.464 ±0.034	4.703 ±0.268	1.669 ±0.095
0702	3.534 ±0.043	1.278 ±0.019	729 (Cu)	2.85 ±0.2	2.65 ±0.1	0.849 ±0.015	1.505 ±0.035	0.536 ±0.040	5.489 ±0.247	1.430 ±0.064
0732	3.568 ±0.052	1.753 ±0.052	741 (Cu)	2.95 ±0.2	2.6 ±0.1	1.170 ±0.032	1.498 ±0.060	0.552 ±0.044	5.650 ±0.307	1.389 ±0.075
0733	3.540 ±0.045	1.775 ±0.043	918 (Cu)	4.1 ±0.3	3.8 ±0.1	1.105 ±0.029	1.606 ±0.057	0.721 ±0.059	6.242 ±0.464	1.222 ±0.091
0737	3.496 ±0.047	1.039 ±0.032	1046 (Cu)	6.2 ±0.4	4.2 ±0.2	0.570 ±0.026	1.823 ±0.100	0.973 ±0.084	7.498 ±0.881	1.047 ±0.123
0738	3.514 ±0.044	1.412 ±0.041	1061 (WHA)	8.5 ±0.5	5.5 ±0.2	0.595 ±0.020	2.373 ±0.105	1.019 0.076	6.159 ±0.410	1.275 ±0.085
0742	3.543 ±0.057	1.351 ±0.039	947 (WHA)	7.3 ±0.3	5.1 ±0.2	0.609 ±0.028	2.135 ±0.116	0.965 ±0.068	6.465 ±0.484	1.214 ±0.091

[a]Flyer material.
[b]Propagated stress is unavailable due to the cutoff of stress trace.

powder compact, it reflects off this interface and re-enters the input gauge package, producing reverberations on the recorded voltage trace for ~130 ns [see Figs. 9(a) and 9(b)]. The reverberation time depends on the wave velocity, the thickness of interface or gauge package, and the difference in shock impedance at both sides of the interface. Similarly, as the forward-going shock wave propagates through the compact/PMMA interface, a weak reshock wave, resulting from the slightly higher impedance of PMMA backer than

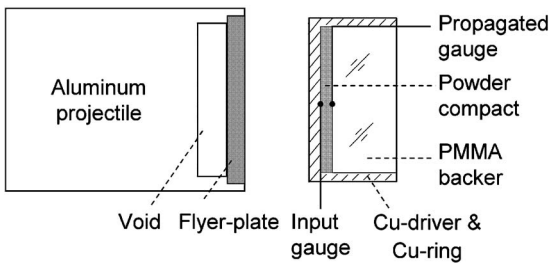

FIG. 7. Schematic of experimental configuration for Hugoniot measurements using piezoelectric stress gauges sandwiching prepressed powder compact for recording the input and propagated stress profiles and shock wave velocity.

that of ~35% TMD nano-Fe powder compact at the loaded stress, is simultaneously reflected off the interface, which recompresses the powder compact and produces reverberations on the recorded voltage trace for ~80 ns [see Figs. 9(c) and 9(d)]. The input stress wave finally approaches the propagated stress wave magnitude as the shock travels back and forth through the powder compact between the Cu driver and PMMA backer [see Fig. 8(a)]. For the ~35% TMD powder compact, the reshock wave reflected off the PMMA backer is steady with increasing shock loading [see Fig. 8(a)], and its magnitude approximately approaches that of the propagated stress wave after a few wave reverberations, suggesting that the moderate load used for pressing the powder to ~35% TMD does not necessarily influence the subsequent dynamic shock loading response of the input gauge. However, in the case of the Hugoniot experiments performed on the ~45% TMD nano-Fe powder compact, the higher load needed for pressing powder can influence and potentially damage the subsequent shock response of the input gauge if the powder is directly pressed into the Cu driver and ring assembly with the input gauge already epoxy mounted onto the driver plate. Thus, we pressed the powder by using

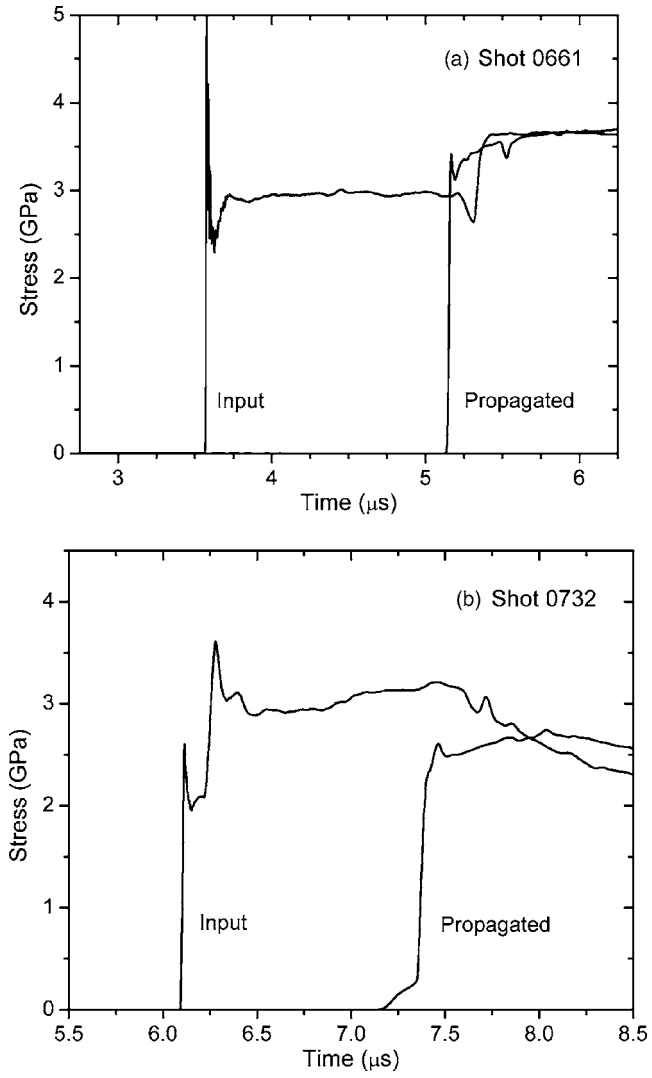

FIG. 8. Measured representative stress profiles obtained by the respective input and propagated gauges for (a) ~35% TMD compact, shot 0661 and (b) ~45% TMD compact, shot 0732.

a steel punch-and-die set, and then placed the ~45% TMD nano-Fe powder compact onto the Cu-driver ring assembly with the input stress gauge premounted onto the driver plate. The presence of an unavoidable gap (~90 μm) between the powder compact and Cu driver resulted in the free surface movement under shock loading and possible damage of the input gauge to a certain degree during the drastic release from peak shock pressure to ambient state. In all experiments (except for shot 0702), the ~45% TMS prepressed nano-Fe powder compact was epoxy bonded between the Cu driver and the PMMA backer to avoid the presence of any air gap. Again, as shown in Fig. 8(b), the input gauge stress pulse obtained for shot 0732 illustrates step loading with the plateau at ~2 GPa representing the stress in the thin epoxy layer (consistent with calculations based on the measured impact velocity) and the corresponding Hugoniot of Cu (impactor and driver plates) and epoxy. The next stress plateau then represents the actual stress amplitude in the powder compact.

In general, as illustrated in Fig. 9, the input stress traces have a short rise time, which is of the order tens of nanoseconds. The propagated gauge (backer) stress profiles in compacts of ~35% TMD have a slightly longer rise time than those recorded by the input stress gauges due to dispersion effects associated with wave propagation through the powder. The propagated stress traces for the compacts of ~45% TMD, however, show a relatively longer rise time, again possibly due to the epoxy bond between the powder compact and the PMMA backer.

Table II lists the relevant data for each experiment performed including the initial powder compact density (ρ_{00}), compact thickness (Δh), and impact velocity (W). The table also includes data obtained from the measured stress gauge records, the input stress ($\sigma_{x,\text{input}}$), and propagated stress ($\sigma_{x,\text{prop}}$) determined based on the criteria described above. The shock transit time (Δt) through the powder thickness (Δh) was calculated based on considering the time interval between the arrival of the wave at the two gauge locations (less time of travel through gauge package thickness). The

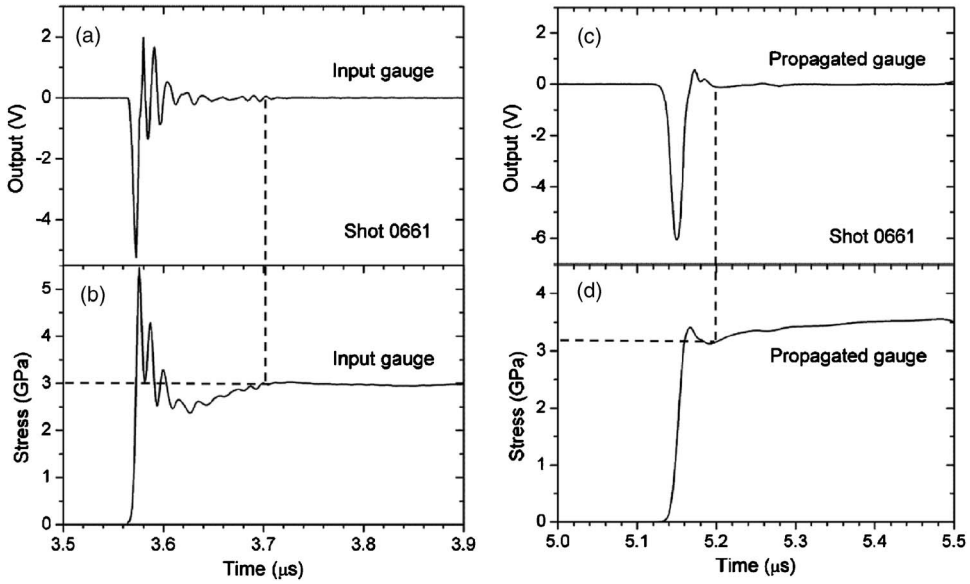

FIG. 9. Example of a typical voltage and stress trace obtained from input and propagated (backer) stress gauges for shot 0661, illustrating the technique for determining equilibrated stress values; (a) and (b) are, respectively, the voltage and stress traces from input stress gauge, and (c) and (d) are, respectively, the voltage and stress traces from propagated stress gauge.

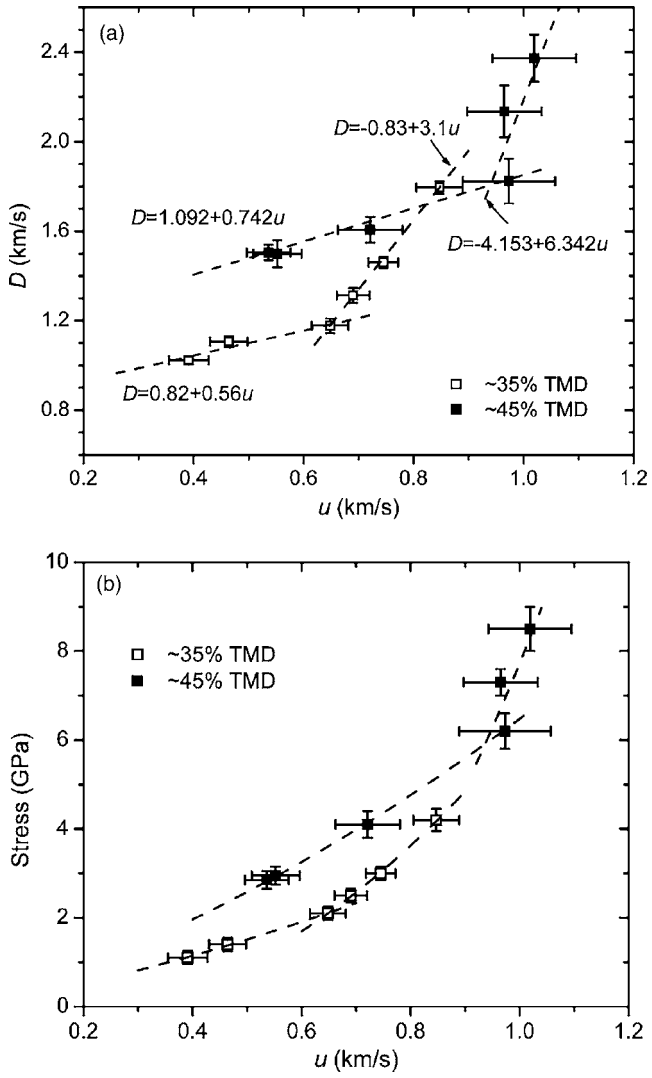

FIG. 10. Measured Hugoniot data for nano-Fe powder compacts of ~35% and ~45% TMD: (a) plot of shock wave velocity (D) against particle velocity (u) and (b) plot of shock stress against particle velocity (u).

shock propagation velocity (D) was determined by averaging the transit time (Δt) at three locations corresponding to ~10%, ~50%, and ~90% of maximum input and propagated stress amplitudes. The maximal deviation in the average from the three transit times was regarded as the uncertainty of Δt. The overall method to evaluate uncertainty for each measured value is described in more detail in the Appendix. The last three columns in Table II include particle velocity (u), shock-compressed state density (ρ), and relative volume (V/V_0), which were calculated by considering the jump conditions and the measured values of shock stress and wave velocity. The particle velocity (u) was determined by using $u=\sigma_x/(\rho_{00}D)$,[21] and the compressed-state density (ρ) was obtained by using $\rho=\rho_{00}D/(D-u)$.[21]

The measured wave velocity D and input stress σ_x are, respectively, plotted against the calculated particle velocity u in Figs. 10(a) and 10(b), respectively. As shown in Fig. 10(a), the D-u line for ~35% TMD nano-Fe compact consists of two distinct segments;

$$D = 0.82 + 0.56u \quad \text{for} \sim 0.35 \text{ km/s} < u \leqslant \sim 0.65 \text{ km/s},$$

$$D = -0.83 + 3.1u \quad \text{for} \sim 0.65 \text{ km/s} < u < \sim 0.9 \text{ km/s}. \tag{11}$$

Likewise, for the ~45% TMD nano-Fe compact, the two segments include

$$D = 1.092 + 0.742u \quad \text{for} \sim 0.4 \text{ km/s} < u < \sim 0.95 \text{ km/s}$$

$$D = -4.153 + 6.342u \quad \text{for} \sim 0.95 \text{ km/s} < u \leqslant \sim 1.1 \text{ km/s}. \tag{12}$$

The stress corresponding to the transition of the two $D(u)$ linear segments is ~2 GPa for ~35% TMD and ~6 GPa for ~45% TMD. The values of shock wave velocity extrapolated to ambient pressure are ~0.8 km/s for ~35% TMD compact and ~1.1 km/s for ~45% TMD compact, which are very close to the measured sound speed values. The deviation of $D(u)$ relation in the range of lower stresses from that in the range of higher stresses is expected because the $D(u)$ relation at higher stresses will result in a negative intercept (C_0) on the $D(u)$ plot, which approximately corresponds to the bulk sound velocity and thus is physically meaningless. The negative C_0 and greater S [the slope on the $D(u)$ plot] in the range of higher stresses are possibly a result of thermal effects or an inhomogeneous mode of deformation, such as strain localization along shear bands. Figure 10(b) shows a higher shock impedance for the ~45% TMD compact than that of the ~35% TMD compact, as expected.

It should be noted that the extracted shock state quantities from the observed stress profiles are based on the jump conditions.[4,6] For the purpose of assessing the stability of the shock wave propagating through the nano-Fe powder compacts, we also calculated the $D(\sigma_x)$ curve based on the jump conditions and compared it to (D,σ_x) data sets directly measured in experiments. The "jump conditions"[4,6] were used to derive the following equation, which was employed to evaluate shock wave velocity D at any given shock stress σ_x:

$$D = C_0/2 + (C_0^2 + 4S\sigma_x V_{00})^{1/2}/2. \tag{13}$$

The calculated $D(\sigma_x)$ data are displayed in Fig. 11, in comparison to the directly measured (D,σ_x) data sets in experiments. It is found that the calculated results based on the jump conditions are consistent with the directly measured data, implying that the observed shock state is quasisteady and the use of the jump conditions is appropriate as an approximation for extracting other quantities from measured stress traces for the ~35% and ~45% TMD nano-Fe powder compacts.

The measured $\sigma_x - V/V_0$ Hugoniot, together with the quasistatic data for the ~35% TMD and ~45% TMD prepressed powder compacts plotted in Fig. 12, shows an obvious transition in specific volume from compression to expansion with increasing shock stress. The lower and upper segments of both Hugoniots are calculated by using their corresponding $D(u)$ relations given in Eqs. (11) and (12). The two segments were smoothly connected for the continuity of shock stress. We assume that the compaction wave in the incomplete compaction region is in thermodynamic equi-

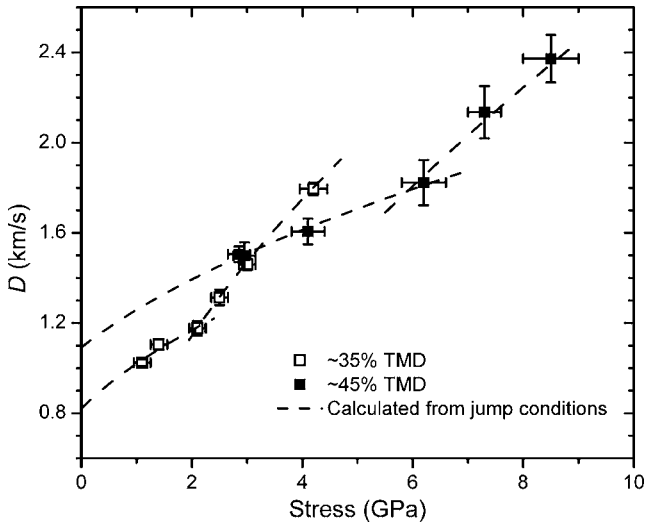

FIG. 11. Plot of measured shock wave velocity (D) against measured shock stress for ~25 nm Fe compacts of ~35% and ~45% TMD.

librium and the strength of compact is negligible; the slope of $\sigma_x - V/V_0$ is of the same expression as that in the complete compaction region,[13] which can be expressed as

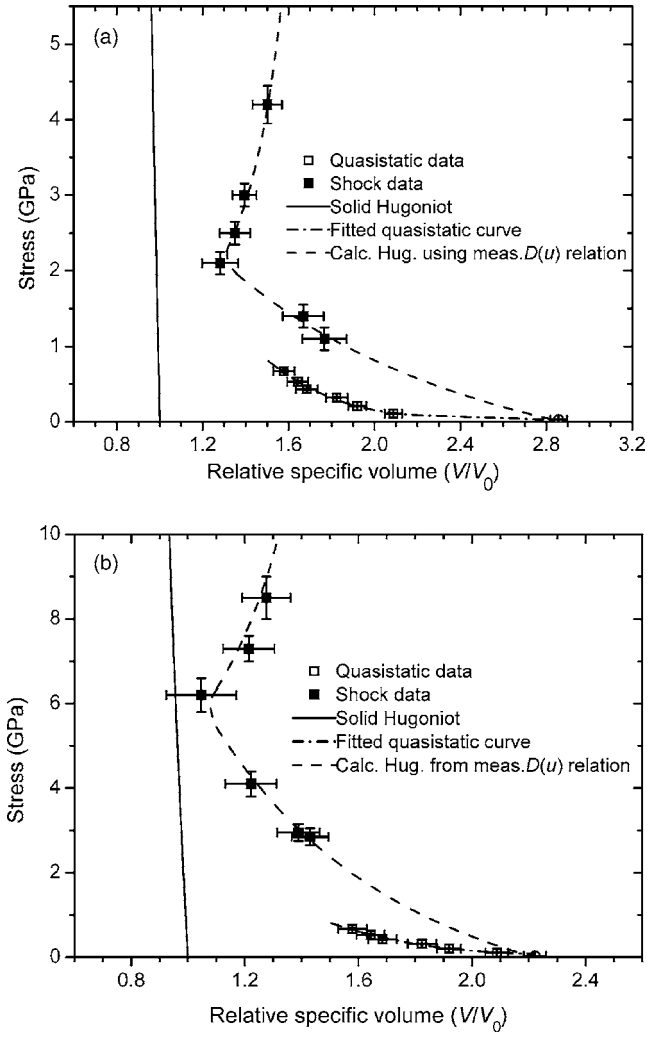

FIG. 12. Plot of measured shock stress vs relative specific volume (V/V_0) for the ~25 nm Fe powder compact together with quasistatic data: (a) ~35% TMD compact and (b) ~45% TMD compact.

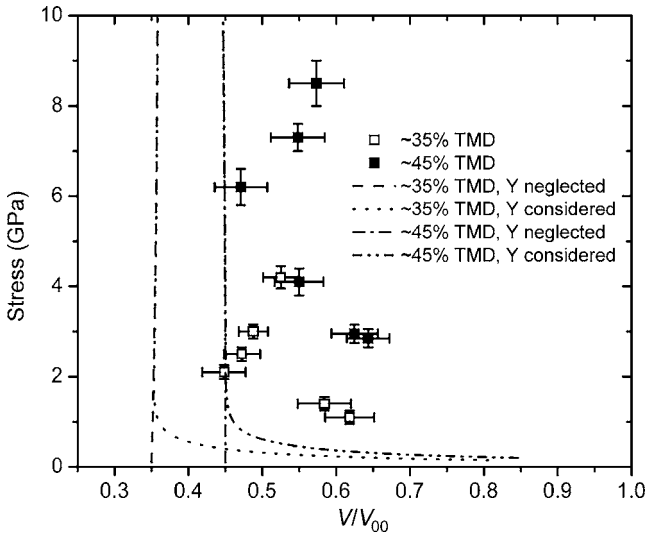

FIG. 13. Comparison of experimental data to results from model calculations using the Wu–Jing method.

$$(dV/d\sigma)_H\big| = [V_{00} - (1 + 2/\gamma)V]/[2C_p/(\alpha V) - \sigma], \qquad (14)$$

where V_{00} is the initial density of powder compact, γ is the Grüneisen parameter under shock compression, C_p is the constant-pressure specific heat, and α is the bulk expansion coefficient. By utilizing the condition of the existence of inflection, namely, $(dV/d\sigma)_H\big|_{V=V_i}^{\sigma=\sigma_i}=0$ (where subscript H denotes the derivative along the Hugoniot and σ_i and V_i are the shock stress and specific volume at the inflection i, respectively), we have $V_i/V_0=(V_{00}/V_0)\gamma/(\gamma+2)$, which yields $V_i/V_0 \approx 1.3$ for ~35% TMD nano-Fe and $V_i/V_0 \approx 1.02$ for ~45% TMD [$\gamma \approx \gamma_0 = 1.69$ for Fe (Ref. 17) in the range of experimental stress], which are in good agreement with the experimental results within the uncertainty of measurements (see Fig. 12). The compression-expansion transition is mainly attributed to the higher porosity of the starting powder compact and compressional heating,[20,21] associated with void collapse. Figure 12 also shows that the measured Hugoniot drastically deviates from the quasistatic data even at lower shock stresses, which is not unexpected due to the difference in stress-loading rate and the higher strain-rate sensitivity of bcc-Fe.

We calculated the Hugoniots of 35% ($\alpha_0 \approx 2.86$) and 45% TMD ($\alpha_0 \approx 2.22$) nano-Fe powder compact by using the Wu–Jing method (the method of McQueen *et al.* is not effective for the high porosities of the compacts) and compared it with the experimental results to examine the applicability of this model for predicting the Hugoniot of nano-Fe powder. We considered two cases in the model calculations: (a) neglecting the powder strength [Eq. (10)] and (b) considering the strength [Eq. (6)]. For case (a), Y and P_E were assumed to be negligible ($Y \approx 0$ and $P_E \approx 0$). For case (b), Y was treated as the strength of nanoparticle grains and P_E was obtained from the measured input stress traces. The calculated $\sigma_x - V/V_{00}$ curves are shown in Fig. 13, indicating that the calculated Hugoniot for both cases using the Wu–Jing approach is not consistent with the measured data. The principal cause for the ineffectiveness of the Wu–Jing method is most possibly the neglect of the characteristic properties of

Fe nanoparticles, in particular, the contribution of the very large specific surface energy associated with the internal energy of the system.[24] The applicability of the Wu–Jing method for predicting the Hugoniot nanopowder compact can possibly be improved by incorporating the difference in internal energy between the powder compact and the solid, and the size effect of nanoparticles on lattice vibrations as they relate to the Grüneisen parameter. The experimental data obtained in this work are particularly valuable for probing the shock densification of Fe nanopowder, for validating the models for nanopowder Hugoniot prediction, and for modeling the complete EOS of iron over a relatively wide range of initial density and temperature.

V. SUMMARY

We have reviewed two representative models of isochoric (McQueen *et al.*) and isobaric (Wu–Jing) approaches for predicting the Hugoniot of highly porous materials (low-density powder compacts) and showed the decreasing accuracy of the two models in predicting the Hugoniot with increasing porosity by comparing the predicted results with available experimental data. The method of McQueen *et al.* becomes insufficient as the porosity of porous materials increases to the critical porosity of $1+2/\gamma_0$, whereas the Wu–Jing method is still effective as the porosity is over the critical value. We have also measured the Hugoniots for ~25 nm Fe powder compacts of ~35% TMD and ~45% TMD by using piezoelectric stress gauges. The experimental data show that the Hugoniot of both highly porous solids (powder compacts) consists of two segments with a densification-distension transition occurring at ~2 GPa for ~35% TMD compact and ~6 GPa for ~45% TMD compact. The experimental data also show a higher shock impedance of ~45% TMD compact than that of ~35% TMD. Comparison of model predictions with experimental measurements shows that the nano-Fe powder Hugoniot cannot be predicted by using the Wu–Jing method, which is otherwise capable of predicting the Hugoniot of highly porous materials (or low-density compacts) of micron-sized powders.

ACKNOWLEDGMENTS

The authors thank M. Martin, A. Fredenburg, L. Ferranti, C. Neel, C. Wehrenberg, P. Draa, A. Siddiqi, J. Crawford, and J. Amato for their assistance with experiments and gas gun operation. This work is supported by ONR/MURI Program Nos. N00014-05-1-0497 and N00014-07-1-0740.

APPENDIX: HUGONIOT DATA UNCERTAINTY EVALUATIONS

1. UNCERTAINTY OF COMPACT DENSITY (ΔP_{00})

The initial density of powder compact is calculated by using

$$\rho_{00} = m/V, \tag{A1}$$

where m and V are the mass and volume of the powder compact, respectively. V is also expressed as

$$V = \pi(d/2)^2 \Delta h, \tag{A2}$$

where d and Δh are the diameter and thickness of the powder compact, respectively. Because m, d, and Δh are independently measured, the uncertainty of ρ_{00} can be expressed as

$$\delta\rho_{00} = \sqrt{\left(\frac{\partial\rho_{00}}{\partial m}\right)^2(\delta m)^2 + \left(\frac{\partial\rho_{00}}{\partial d}\right)^2(\delta d)^2 + \left(\frac{\partial\rho_{00}}{\partial\Delta h}\right)^2(\delta\Delta h)^2}, \tag{A3a}$$

where δm, δd, and $\delta\Delta h$ are the uncertainties of m, d, and Δh measurements, respectively; $\partial\rho_{00}/\partial m$, $\partial\rho_{00}/\partial d$, and $\partial\rho_{00}/\partial\Delta h$ are obtained from Eqs. (A1) and (A2) as follows:

$$\frac{\partial\rho_{00}}{\partial m} = \frac{1}{V} = \frac{1}{\pi(d/2)^2\Delta h}, \tag{A3b}$$

$$\frac{\partial\rho_{00}}{\partial d} = -\frac{m}{\pi(d/2)^3\Delta h}, \tag{A3c}$$

$$\frac{\partial\rho_{00}}{\partial\Delta h} = -\frac{m}{\pi(d/2)^2(\Delta h)^2}. \tag{A3d}$$

Inserting Eqs. (A3b) and (A3c) into Eq. (A3a) yields

$$\frac{\delta\rho_{00}}{\rho_{00}} = \sqrt{\left(\frac{\delta m}{m}\right)^2 + \left(\frac{2\delta d}{d}\right)^2 + \left(\frac{\delta\Delta h}{\Delta h}\right)^2}. \tag{A4}$$

2. UNCERTAINTY OF SHOCK WAVE VELOCITY (ΔD)

The shock wave velocity is determined by using

$$D = \Delta h/\Delta t, \tag{A5}$$

where Δh and Δt are the compact thickness and shock wave propagation time through the compact, respectively. Since the Δh and Δt are independently measured, the uncertainty of D can be expressed as

$$\delta D = \sqrt{\left(\frac{\partial D}{\partial\Delta h}\right)^2(\delta\Delta h)^2 + \left(\frac{\partial D}{\partial\Delta t}\right)^2(\delta\Delta t)^2}, \tag{A6a}$$

where $\delta\Delta h$ and $\delta\Delta t$ are the uncertainties of Δh and Δt measurements, respectively. Similarly, $\partial D/\partial\Delta h$ and $\partial D/\partial\Delta t$ are derived from Eq. (A5) as follows:

$$\frac{\partial D}{\partial\Delta h} = 1/\Delta t, \tag{A6b}$$

$$\frac{\partial D}{\partial\Delta t} = -\Delta h/(\Delta t)^2. \tag{A6c}$$

By substituting Eqs. (A6b) and (A6c) into Eq. (6), we have

$$\frac{\delta D}{D} = \sqrt{\left(\frac{\delta\Delta h}{\Delta h}\right)^2 + \left(\frac{\delta\Delta t}{\Delta t}\right)^2}. \tag{A7}$$

3. UNCERTAINTY OF PARTICLE VELOCITY (ΔU)

The particle velocity is calculated by using

$$u = \sigma_x/\rho_{00}D, \tag{A8}$$

where σ_x is the measured shock stress. Because σ_x, ρ_{00}, and D are independently measured, the uncertainty of u can be expressed as

$$\delta u = \sqrt{\left(\frac{\partial u}{\partial \sigma_x}\right)^2(\delta\sigma_x)^2 + \left(\frac{\partial u}{\partial \rho_{00}}\right)^2(\delta\rho_{00})^2 + \left(\frac{\partial u}{\partial D}\right)^2(\delta D)^2}, \tag{A9}$$

where $\delta\sigma_x$, $\delta\rho_{00}$, and δD are uncertainties of σ_x, ρ_{00}, and D measurements, respectively. Similarly, by inserting the expressions of $\partial u/\partial\sigma_x$, $\partial u/\partial\rho_{00}$, and $\partial u/\partial D$, obtained from Eq. (A8) into Eq. (A9), we have

$$\frac{\delta u}{u} = \sqrt{\left(\frac{\delta\sigma_x}{\sigma_x}\right)^2 + \left(\frac{\delta\rho_{00}}{\rho_{00}}\right)^2 + \left(\frac{\delta D}{D}\right)^2}. \tag{A10}$$

4. UNCERTAINTY OF SHOCK-COMPRESSED STATE DENSITY (ΔP)

The shock-compressed state density is calculated by using

$$\rho = \rho_{00}D/(D-u). \tag{A11}$$

The uncertainty in u can be approximately expressed as

$$\delta\rho \approx \sqrt{\left(\frac{\partial\rho}{\partial\rho_{00}}\right)^2(\delta\rho_{00})^2 + \left(\frac{\partial\rho}{\partial D}\right)^2(\delta D)^2 + \left(\frac{\partial\rho}{\partial u}\right)^2(\delta u)^2}. \tag{A12}$$

Similarly, by substituting the expressions of $\partial\rho/\partial\rho_{00}$, $\partial\rho/\partial D$, and $\partial\rho/\partial u$ obtained from Eq. (A11) into Eq. (A12), we acquire

$$\frac{\delta\rho}{\rho} \approx \sqrt{\left(\frac{\delta\rho_{00}}{\rho_{00}}\right)^2 + \left[\left(\frac{u}{D}\right)\left(\frac{\delta D}{D-u}\right)\right]^2 + \left(\frac{\delta u}{D-u}\right)^2}. \tag{A13}$$

5. UNCERTAINTY OF SPECIFIC VOLUME UNDER SHOCK COMPRESSION (ΔV)

The specific volume (V) at shock pressure is related to ρ by $V=1/\rho$. Thus, the uncertainty of V can be expressed as

$$\delta V = \sqrt{\left(\frac{\partial V}{\partial\rho}\right)^2(\delta\rho)^2} = \left|\frac{\partial V}{\partial\rho}\delta\rho\right| = \frac{\delta\rho}{\rho^2}, \tag{A14}$$

from which we have

$$\frac{\delta V}{V} = \frac{\delta\rho}{\rho}. \tag{A15}$$

6. UNCERTAINTY OF RELATIVE SPECIFIC VOLUME ($\Delta A = V/V_0$)

By definition, $\alpha = V/V_0$ (where V_0 is the initial specific volume of polycrystalline solid). We assume that the uncertainty of V_0 is negligible and, thus, the uncertainty of α is approximately expressed as

$$\delta\alpha = \sqrt{\left(\frac{\partial\alpha}{\partial V}\right)^2(\delta V)^2} = \left|\frac{\partial\alpha}{\partial V}\delta V\right| = \frac{\delta V}{V_0}. \tag{A16}$$

The relative uncertainty of α is

$$\frac{\delta\alpha}{\alpha} = \frac{\delta V}{V} = \frac{\delta\rho}{\rho}. \tag{A17}$$

[1] V. F. Nesterenko, *Dynamics of Heterogeneous Materials* (Springer, New York, 2001).
[2] N. N. Thadhani, A. H. Mutz, and T. Vreeland, Acta Metall. **37**, 897 (1989).
[3] Z. Q. Jin, K. H. Chen, J. Li, P. Liu, and N. N. Thadhani, Acta Mater. **52**, 2147 (2004).
[4] J. Colvin, in *Shock Compression of Condensed Matter*, edited by M. Elert, M. D. Furnish, R. Chau, N. Holmes, and J. Nguyen (AIP, New York, 2007), pp. 31–34.
[5] C. D. Dai, D. Eakins, and N. N. Thadhani, Appl. Phys. Lett. **90**, 071911 (2007).
[6] R. G. McQueen, S. P. Marsh, J. W. Taylor, F. N. Fritz, and W. J. Carter, in *High-Velocity Impact Phenomena*, edited by R. Kinslow (Academic, New York, 1970), pp. 293–417.
[7] G. A. Simon and H. H. Legner, J. Appl. Phys. **53**, 943 (1982).
[8] K. H. Oh and P. A. Persson, J. Appl. Phys. **65**, 3852 (1989).
[9] D. K. Dijken and J. T. M. De Hosson, J. Appl. Phys. **75**, 809 (1994).
[10] Q. Wu and F. Q. Jing, J. Appl. Phys. **80**, 4343 (1996).
[11] L. Boshoff-Mostert and H. J. Viljoen, J. Appl. Phys. **86**, 1245 (1999).
[12] W. Hermann, J. Appl. Phys. **40**, 2490 (1969).
[13] M. M. Carroll and A. C. Holt, J. Appl. Phys. **43**, 1626 (1972).
[14] D. E. Grady, *Analytic Solutions and Constitutive Relations for Shock Propagation in Porous Media* (AIP, New York, 2003), pp. 205–208.
[15] T. J. Vogler, M. Y. Lee, and D. E. Grady, Int. J. Solids Struct. **44**, 636 (2007).
[16] R. K. Linde and D. N. Schmidt, J. Appl. Phys. **37**, 3259 (1966).
[17] R. G. McQueen, in *High-Pressure Equation of States: Theory and Applications*, edited by S. Eliezer and R. A. Ricci (North-Holland, Amsterdam, 1991), pp. 101–216.
[18] M. Born and J. Mayer, Z. Phys. **75**, 1 (1932).
[19] S. P. Marsh, *LASL Shock Hugoniot Data* (University California Press, Berkeley, CA, 1980).
[20] R. F. Trunin, *Shock Compression of Condensed Materials* (Cambridge University Press, Cambridge, 1998), pp. 63–76.
[21] Ya. B. Zel'dovich and Yu. P. Raizer, *Physics of Shock Waves and High-Temperature Hydrodynamic Phenomena*, edited by W. D. Hayes and R. F. Probstein (Dover, New York, 2002), pp. 712–716.
[22] X. S. Xu and W. X. Zhang, *Introduction to Theory of Equation of State* (Science, Beijing, 1986), p. 535 (in Chinese).
[23] A. C. Mitchell and W. J. Nellis, J. Appl. Phys. **52**, 3363 (1981).
[24] N. F. Uvarov and V. V. Boldyrev, Russ. Chem. Rev. **70**, 265 (2001).
[25] G. Huayun, W. Qiang, T. Hua, C. Lingcang, and J. Fuqian, J. Appl. Phys. **92**, 5917 (2002).
[26] G. Huayun, W. Qiang, T. Hua, C. Lingcang, and J. Fuqian, J. Appl. Phys. **92**, 5917 (2002).
[27] F. Bauer, IEEE Trans. Ultrason. Ferroelectr. Freq. Control **47**, 1448 (2000).
[28] R. A. Graham, M. U. Anderson, F. Bauer, and R. E. Setchell, in *Piezoelectric Polarization of the Ferroelectric Polymer PVDF from* 10 MPa to 10 GPa*: Studies of Loading-Path Dependence*, Shock Compression of Condensed Matter, edited by S. C. Schmidt, R. Dick, J. Forbes, and D. Tasker (AIP, New York, 1992), p. 883–886.
[29] N. N. Thadhani, R. A. Graham, T. Royal, E. Dunbar, M. U. Anderson, and G. T. Holman, J. Appl. Phys. **82**, 1113 (1997).
[30] K. V. Vandersall and N. N. Thadhani, J. Appl. Phys. **94**, 1575 (2003).
[31] X. Xu and N. N. Thadhani, J. Appl. Phys. **96**, 2000 (2004).
[32] D. Eakins and N. N. Thadhani, J. Appl. Phys. **100**, 113521 (2006).